Heliyon 9 (2023) e16245

Contents lists available at ScienceDirect

Heliyon

journal homepage: www.cell.com/heliyon

Research article

Preparation of core-shell MOF@MOF nanoparticle as matrix for the analysis of rhubarb anthraquinones in plasma by matrix-assisted laser desorption/ionization time-of-flight mass spectrometry

Shi-Jun Yin [a,1], Hua Chen [a,1], Shengpeng Wang [b,**], Yitao Wang [b], Feng-Qing Yang [a,*]

[a] School of Chemistry and Chemical Engineering, Chongqing University, Chongqing, 401331, China
[b] State Key Laboratory of Quality Research in Chinese Medicine, Institute of Chinese Medical Sciences, University of Macau, Macao, China

ARTICLE INFO

Keywords:
Core-shell structure
Metal-organic framework
Laser desorption/ionization
Mass spectrometry analysis
Rhubarb anthraquinone

ABSTRACT

A core-shell structure UiO-66-$(OH)_2$@UiO-66-NH_2 (MOF@MOF) nanoparticle was synthesized through a simple hydrothermal method and employed as an adsorbent and laser desorption/ionization time-of-flight mass spectrometry (MALDI-TOF-MS) matrix for the quantitative analysis of rhubarb anthraquinones (RAs). The properties of the materials were characterized by field emission scanning electron microscopy, transmission electron microscopy, energy-dispersive X-ray spectroscopy, X-ray powder diffraction, Fourier transform infrared spectroscopy, X-ray photoelectron spectroscopy, thermogravimetric analysis, and Brunauer-Emmett-Teller. The results indicate that MOF@MOF is regular octahedral structure with a size distribution of about 100 nm, having large BET specific surface area (920 m^2/g). Using the MOF@MOF as a matrix shows lower background interference, higher sensitivity, and better storage stability than that of traditional matrices. The MOF@MOF matrix exhibits excellent salt tolerance even under a NaCl concentration of 150 mM. Then, the enrichment conditions were optimized, and the adsorption time of 10 min, adsorption temperature of 40 °C and adsorbent amount of 100 μg were selected. In addition, the possible mechanism of MOF@MOF as an adsorbent and matrix was discussed. Finally, the MOF@MOF nanoparticle was employed as a matrix for the sensitive MALDI-TOF-MS analysis of RAs in spiked rabbit plasma, and the recoveries are in the range of 88.3–101.5% with RSD ≤9.9%. In short, the novel MOF@MOF matrix has demonstrated its potential in the analysis of small-molecule compounds in biological samples.

Abbreviations: **AA**, acetic acid; **ACN**, acetonitrile; **CHR**, chrysophanol; **DHB**, 2,5-dihydroxybenzoic acid; **DMF**, dimethyl formamide; **EDX**, energy dispersive X-ray detector; **EMO**, emodin; **FE-SEM**, field emission scanning electron microscopy; **FT-IR**, Fourier transform infrared spectroscopy; **LOD**, limit of detection; **LOQ**, limit of quantification; **MALDI-TOF-MS**, Matrix-assisted laser desorption/ionization time-of-flight mass spectrometry; **MOFs**, metal-organic frameworks; **PHY**, physcion; **PVP**, polyvinyl pyrrolidone; **RAs**, rhubarb anthraquinone; **SA**, sinapic acid; **SNR**, signal-to-noise ratio; **TEM**, transmission electron microscope; **TGA**, thermogravimetric analysis; **THAP**, 2′,4′,6′-trihydroxyacetophenone monohydrate; **TPA-NH_2**, 2-aminoterephthalic acid; **TPA-$(OH)_2$**, 2,5-dihydroxytelephthalic acid; **RSD**, relative standard deviation; **XPS**, X-ray photoelectron spectroscopy.

* Corresponding author. School of Chemistry and Chemical Engineering, Chongqing University, Chongqing, 401331, China.
** Corresponding author.
E-mail addresses: swang@um.edu.mo (S. Wang), fengqingyang@cqu.edu.cn (F.-Q. Yang).
[1] These authors contribute equally to this work.

https://doi.org/10.1016/j.heliyon.2023.e16245
Received 1 October 2022; Received in revised form 4 May 2023; Accepted 10 May 2023
Available online 13 May 2023

1. Introduction

Matrix-assisted laser desorption/ionization time-of-flight mass spectrometry (MALDI-TOF-MS), owing to its advantages, including high throughput, low fragmentation, no cross-contamination, and high sensitivity, has become a powerful tool for the analysis of macromolecules such as proteins [1], peptides [2], oligonucleotides [3], and synthetic polymers [4]. However, the MALDI-TOF-MS has obvious limits in the analysis of small molecules. The strong background interference induced by the self-dissociation of traditional organic matrices in the low-mass region, and the "sweet spot" effect resulted from the heterogeneous mixing and co-crystallization of analyte and matrix molecules, leading to the poor repeatability and unreliable of the test results [5]. Therefore, many novel matrices, such as carbon-based materials [6], silica-based materials [7], and metallic materials [8], have been reported for the analysis of small molecules. They can not only minimize the background noise at the small-molecule scale, but also improve the ionization efficiency by taking the advantage of synergistic effects of components in the nanomaterial. However, there are some inherent defects in different nanomaterial substrates. For example, carbon materials are difficult to be dispersed and silicon materials have poor reproducibility. Thus, the development of new matrix for the MALDI-MS analysis of small molecules is appealing [9–11].

As a class of porous and crystalline functional materials, metal-organic frameworks (MOFs), consisted of metal ions or metal clusters and organic ligands, had been widely applied in the fields of gas separation [12], energy storage [13], and catalysis [14], owing to their unique properties, such as high surface area, numerous active sites, and high porosity [15]. Furthermore, MOFs has high molar absorption coefficient in the UV–visible range that can effectively absorb laser energy. Additionally, MOFs can form a uniform solid with the analyte and transfer energy to the analyte or induce its ionization. These properties make MOFs become an ideal matrix for MALDI-TOF-MS analysis. Especially, the core-shell structure MOF@MOF can maintain the chemical, physical, and structural advantages of both MOFs but generate new synergistic effects [16]. In addition, core-shell structure MOF material with the characteristics of high specific surface area and abundant active sites, can realize the effective pre-concentration of low concentration analytes before the MALDI-TOF-MS analysis.

Emodin (EMO), chrysophanol (CHR), and physcion (PHY) are the main active anthraquinone (RAs) components in traditional Chinese medicine rhubarb, which have several pharmacological activities, such as antibacterial [17], antiviral [18], anti-inflammatory [19], inhibiting pulmonary fibrosis, and protecting intestinal mucosal barrier [20]. Several methods have been reported for the analysis of RAs, including thin layer chromatography (TLC) [21], HPLC [22], HPLC-Q-TOF-MS [23], and capillary electrophoresis (CE) [24]. However, MALDI-TOF-MS based analysis for the detection of RAs has not been reported. The anthraquinone structure and rich phenolic hydroxyl groups in RAs may produce strong interaction with MOF@MOF material. Therefore, RAs were selected as representative small-molecule compounds in the quantitative analysis by MALDI-TOF-MS.

In this work, a core-shell UiO-66-$(OH)_2$@UiO-66-NH_2 material (MOF@MOF) was synthesized through a solvothermal method and employed as an adsorbent and matrix to achieve enrichment and quantitative analysis of RAs by MALDI-TOF-MS. The prepared material exhibits high salt tolerance and long-term storage stability, and can be used for rapid analysis of many types of small-molecule compounds with very low background interference. Furthermore, under the optimized conditions, a quantitative MALDI-TOF-MS method by using MOF@MOF as matrix for the analysis of RAs was developed and validated. Finally, the developed method was applied in the determination of RAs in spiked rabbit plasma sample.

2. Materials and methods

2.1. Chemicals and regents

Sodium chloride (NaCl, ≥99.5%), dimethyl formamide (DMF, ≥99.5%), and acetic acid (AA, >99.5%) were purchased from Chengdu Chron Chemicals Co., Ltd. (Chengdu, China) (http://www.chronchem.com/en/). The 2-aminoterephthalic acid (TPA-NH_2, ≥98%) was purchased from Shanghai DiBai Biological Technology Co., Ltd. (Shanghai, China) (http://www.chemxyz.com/). Zirconyl chloride hydrate ($ZrOCl_2{\cdot}H_2O$, ≥99.99%) was purchased from Beijing Mreda Technology Co., Ltd. (Beijing, China) (http://www.ouhetech.com/). Emodin (≥98%), chrysophanol (≥98%), physcion (≥98%), and psoralen (≥99%) was purchased from Chengdu DeSiTe Biological Technology Co., Ltd. (Chengdu, China) (http://cddesite.foodmate.net/), and their chemical structures are shown in Fig. S1. Phenylalanine (>98%) and acetonitrile (ACN, HPLC-grade) were purchased from Adamas-beta (Shanghai, China) (http://www.adamas-beta.com). Hesperetin was purchased from TargetMol, (USA) (www.targetmol.com). Polyvinyl pyrrolidone (PVP, MW = 40000), rabbit plasma (heparin sodium as anticoagulant), tyrosine (>99%), glutamic acid (>99%), and histidine (>99%) were purchased from Shanghai YuanYe Biological Technology Co., Ltd. (Shanghai, China) (http://yuanyebio.bioon.com.cn/). Zirconium tetrachloride ($ZrCl_4$, ≥99.9%), 2,5-dihydroxytelephthalic acid (TPA-$(OH)_2$, ≥98%), 2,5-dihydroxybenzoic acid (DHB, >99%), sinapic acid (SA, >98%), and 2′,4′,6′-trihydroxyacetophenone monohydrate (THAP, 98%) were purchased from Shanghai Aladdin Biochemical Technology Co., Ltd. (Shanghai, China) (https://www.aladdin-e.com/). Naringenin (>98%), rosmarinic acid (>98%), and tanshinone IIA (>98%) were purchased from Chengdu HerbSubstance Co., Ltd. (Chengdu, China) (https://www.herbsubstance.com/). Water used for all the experiments was purified by a water purification system (ATSelem 1820A, Antesheng Environmental Protection Equipment Co., Ltd., Chongqing, China) (http://www.atshb.com/). The other instrumental information is shown in the ESM.

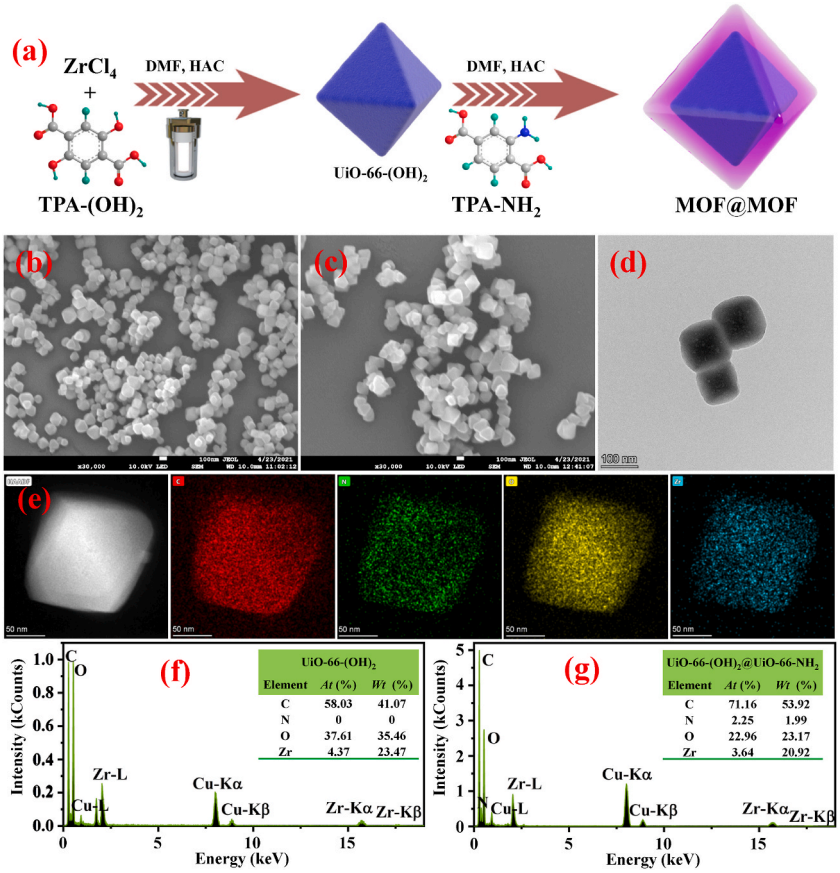

Fig. 1. (**a**) Schematic diagram of the preparation of UiO-66-$(OH)_2$@UiO-66-NH_2; SEM images of (**b**) UiO-66-$(OH)_2$ and (**c**) UiO-66-$(OH)_2$@UiO-66-NH_2; (**d**) TEM image and (**e**) elemental mapping images of UiO-66-$(OH)_2$@UiO-66-NH_2; EDS results of (**f**) UiO-66-$(OH)_2$ and (**g**) UiO-66-$(OH)_2$@UiO-66-NH_2.

2.2. Preparation of UiO-66-$(OH)_2$@UiO-66-NH_2

The MOF@MOF nanoparticle was prepared by a facile two-step process and the schematic diagram of the material synthesis process is shown in Fig. 1a. Firstly, UiO-66-$(OH)_2$ was prepared [25]. In brief, 168.0 mg of $ZrCl_4$, 142.8 mg of TPA-$(OH)_2$, and 159.5 mg of PVP were ultrasonically dissolved in 12.2 mL of DMF. Then, 10.2 mL of AA and 0.4 mL of deionized water were added and stirred at room temperature for 10 min. After that, the mixture solution was transferred to a 50 mL Teflon-lined autoclave and heated to 120 °C for 2 h. The white product was washed twice by DMF and ethanol, followed by vacuum drying at 60 °C for 8 h.

For the preparation of core-shell structure UiO-66-$(OH)_2$@UiO-66-NH_2, 108.8 mg of TPA-NH_2 and 42.0 mg of $ZrOCl_2{\cdot}H_2O$ was dissolved in 12.0 mL of DMF and 8.0 mL of AA. Then, 100.0 mg of obtained UiO-66-$(OH)_2$ powder was added in the solution and treated by ultrasonication for 10 min. After that, the mixture solution was continuously stirred at 90 °C for 4 h. The product was washed twice by DMF and ethanol, followed by vacuum drying at 60 °C for 8 h. The instruments and conditions for characterization of the materials are presented in the ESM.

2.3. Preparation of MALDI matrices and MALDI-TOF-MS analysis

The traditional matrices, such as DHB, SA, and THAP, were prepared as saturated solutions in ACN/water (1:1, v/v) containing 0.1% trifluoroacetic acid at the final concentration of 10 mg/mL in analytes' solutions, respectively. For the preparation of MOF@MOF stock solution, the MOF@MOF matrix was dispersed in ACN to form homogeneous solution at the concentration of 1.0 mg/mL. Enrichment operations are as follows: 0.1 mL of MOF@MOF solution was added in a 2-mL centrifuge tube containing 0.9 mL of tested sample solution and shaken on a temperature-controlled air bath shaker at 150 rpm for 10 min under 40 °C to acquire adequate adsorption. Then, the material was separated by centrifugation at 4316×*g* for 5 min and re-dispersed in 50 μL of ACN under ultrasonication. Finally, 1 μL of analysis solution was dropped onto the MALDI stainless steel plate and dried at room temperature before MALDI-TOF-MS analysis. The detailed method of storage stability, salt tolerance, and applicability are described in the ESM.

The MALDI-TOF-MS analysis was performed on a MALDI-7090 equipped with a pulsed nitrogen laser (355 nm) in reflection and positive ion mode. The instrumental parameters are as follows: raster type, regular circle; profiles, 100 profiles; accumulate, 50shot(s)

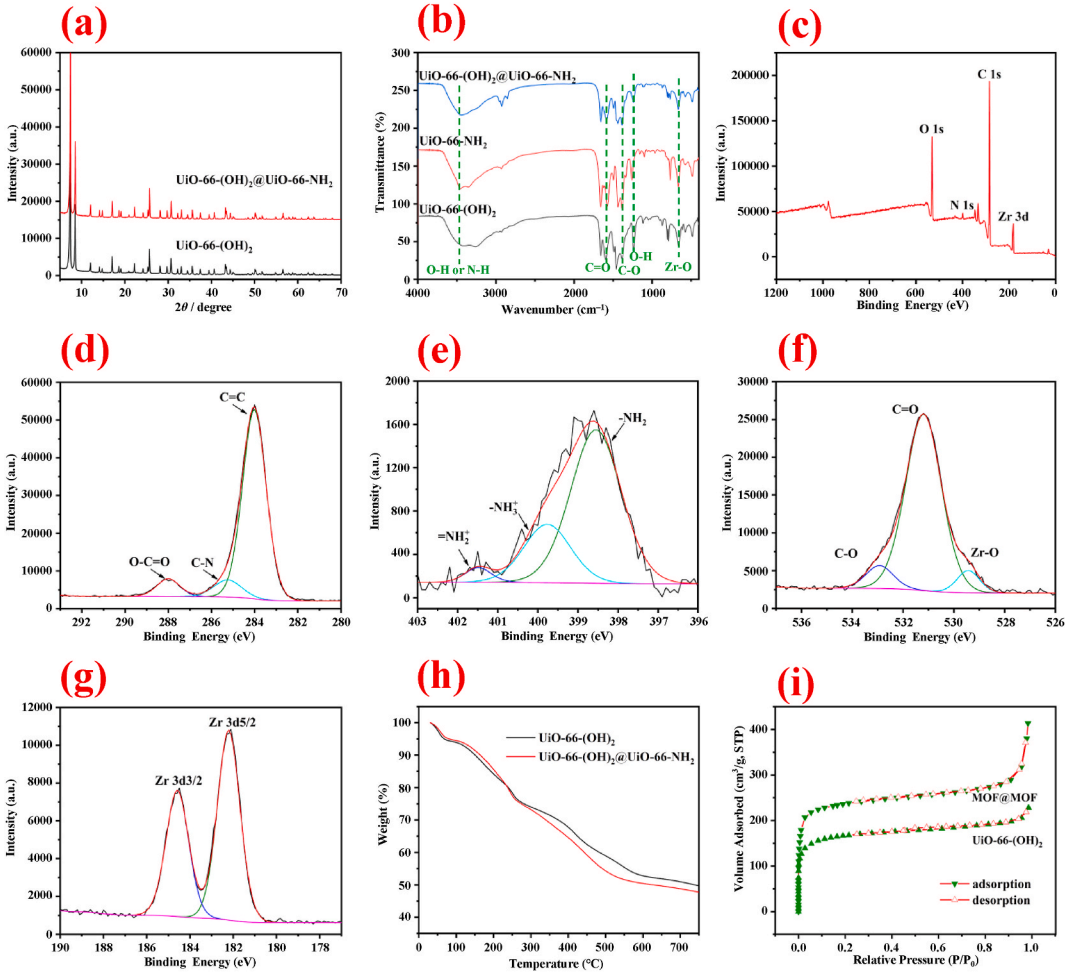

Fig. 2. (**a**) The XRD spectra of UiO-66-$(OH)_2$ and UiO-66-$(OH)_2$@UiO-66-NH_2; (**b**) The FT-IR spectra of UiO-66-$(OH)_2$, UiO-66-NH_2, and UiO-66-$(OH)_2$@UiO-66-NH_2; The XPS spectra of UiO-66-$(OH)_2$@UiO-66-NH_2: (**c**) full spectrum, (**d**) C 1s, (**e**) N 1s, (**f**) O 1s, (**g**) Zr 3 d; (**h**) The TGA result and (**i**) nitrogen adsorption-desorption isotherm of UiO-66-$(OH)_2$ and UiO-66-$(OH)_2$@UiO-66-NH_2.

@50Hz. A polished-steel sample target with 384 spots was employed and the laser intensity was adjusted to 30%. All mass spectra were analyzed by Mass++ (64-bit) software (Shimadzu Scientific Instruments, Kyoto, Japan).

2.4. Solid-phase extraction procedure

For the solid-phase extraction procedure, 2.0 mg of adsorbent was added in a 2-mL centrifuge tube containing 1.0 mL of 20 μg/mL of RAs solutions (dissolved in ACN) and shaken at 150 rpm for 10 min under 40 °C to acquire adsorption equilibrium. Then, the supernatant was filtered through a 0.22 μm filter before HPLC analysis. Detailed HPLC analysis conditions are described in the ESM.

2.5. UV–Vis analysis of MOF@MOF solution

In brief, 0.1 mL of MOF@MOF (dispersed in ethanol, 1.0 mg/mL) was mixed well with 1.9 mL of deionized water (final concentration of 50 μg/mL), and the absorbance in the range of 250–800 nm was recorded [26].

3. Results and discussion

3.1. Characterization of the MOF materials

Fig. 1b and c shows the field emission scanning electron microscopy (FE-SEM) images of the synthesized UiO-66-$(OH)_2$ and UiO-66-$(OH)_2$@UiO-66-NH_2. In the observation, both are well-dispersed and exhibit regular octahedral structures with a smooth surface. Although UiO-66-NH_2 modification was conducted at atmospheric pressure, MOF@MOF can maintain a regular morphology. As the

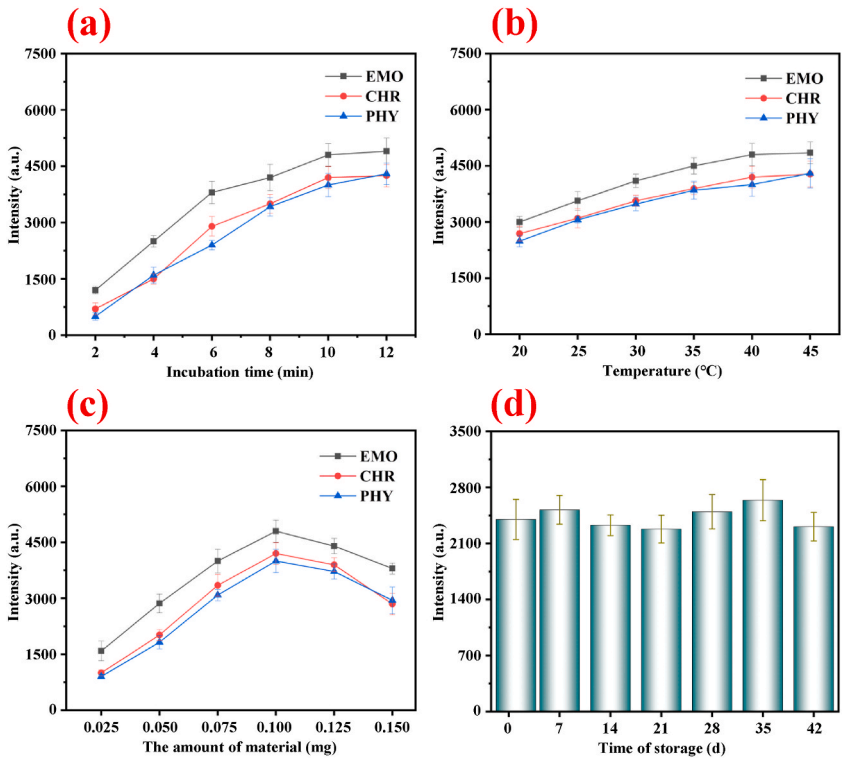

Fig. 3. The effect of (**a**) incubation time, (**b**) temperature, (**c**) the amount of material and (**d**) storage stability of UiO-66-$(OH)_2$@UiO-66-NH_2 on the intensity of emodin ($[M+H]^+$ at m/z 271, 250 ng/mL) ($n = 3$).

transmission electron microscope (TEM) result shown in Fig. 1d, MOF@MOF has regular facets with a size distribution of about 100 nm. From the element mapping images in Fig. 1e, the C, N, O, and Zr elements are uniformly distributed in the MOF@MOF. In addition, from the energy dispersive X-ray detector (EDX) spectra in Fig. 1f and g, the appearance of N element further supports the successful synthesis of the core-shell MOF@MOF.

X-ray diffraction was employed to determine the crystal structure of UiO-66-$(OH)_2$ and MOF@MOF. The X-ray diffraction patterns (Fig. 2a) presence five main peaks at a 2θ values of 7.35°, 8.48°, 17.04°, 25.65°, and 30.64°, belonging to the crystal planes of (1 1 1), (2 0 0), (4 0 0), (6 0 0), and (7 1 1), respectively, which is consistent with those reports of UiO-66-NH_2 and UiO-66-$(OH)_2$ [27,28]. All the materials are highly crystalline, and the modification of UiO-66-NH_2 does not change the intrinsic crystal structure of the core UiO-66-$(OH)_2$.

The Fourier transform infrared spectroscopy (FT-IR) spectra of UiO-66-$(OH)_2$, UiO-66-NH_2, and MOF@MOF are shown in Fig. 2b. The peaks' positions in the FT-IR spectra of the three materials are similar, which further indicate that the types of functional groups do not change significantly during the modification process. The broad absorption peak at 3200–3500 cm^{-1} is attributed to the N–H or O–H bond stretching vibration [29]. The adsorption peak at 1582 cm^{-1} is the C═O stretching vibration of the carboxyl group [30]. Furthermore, the adsorption peak at 1387 cm^{-1} is corresponded to the C–O stretching vibration, and the adsorption peak at 1238 cm^{-1} is assigned to the stretching vibration of phenolic hydroxyl group [31]. In addition, the adsorption peak at 666 cm^{-1} is related to the stretching vibration of Zr–O [29].

To analyze the chemical state of the material, the X-ray photoelectron spectroscopy (XPS) spectra of MOF@MOF are recorded and the results are shown in Fig. 2c–g. It can be observed from Fig. 2c that the C, O, N, and Zr elements exist in the MOF@MOF. From Fig. 2d, C 1s spectrum can be divided into three peaks, which are assigned to the O–C═O (288.2 eV), C–N (285.3 eV), and C═C (284.0 eV), respectively [32]. In the XPS spectrum of N 1s (Fig. 2e), the peaks located at 401.5 eV, 399.8 eV, and 398.6 eV can be attributed to the = NH2 +, -NH3 +, and –NH_2, respectively [33]. Furthermore, the O 1s spectrum (Fig. 2f) is centered at 532.9 eV, 529.4 eV, and 531.2 eV, which indicate the existence of C–O, C═O, and Zr–O [34], respectively. In addition, the binding energy of Zr 3d3/2 and Zr 3d5/2 (Fig. 2g) are assigned to 184.7 eV and 182.2 eV, respectively [35].

To understand the thermal properties of the synthesized materials, the thermogravimetric analysis (TGA) analysis was carried out. From the TGA profiles displayed in Fig. 2h, UiO-66-$(OH)_2$ and MOF@MOF exhibit similar thermal property. At the temperature below 100 °C, a weight loss of around 5.9% is related to the evaporation of water that is physically attached on the material surface. Furthermore, in the temperature range of 110–200 °C, a weight loss (12.1%) was occurred due to the evaporation of ethanol and the decomposition of DMF trapped in the frameworks. The subsequent weight loss at higher temperature may be attributed to the collapse of the skeleton, i.e. TPA-NH_2 and TPA-$(OH)_2$ decompositions [36].

The N_2 adsorption-desorption isotherms (Fig. 2i) of UiO-66-$(OH)_2$ and MOF@MOF were investigated. The adsorption isotherms

rise straightly at low pressure and quickly reach a saturation. The N_2 adsorption-desorption isotherms are the typical Type I isotherm of microporous feature. Both samples have large BET specific surface area of 677 and 920 m^2/g with the total pore volume of 0.35 and 0.64 cm^3/g for UiO-66-$(OH)_2$ and MOF@MOF, respectively [37].

3.2. The feasibility of using MOF@MOF as a matrix in MALDI-TOF-MS analysis

The ideal MALDI matrix should have the following characteristics. 1) It has good light absorption and transmission ability to laser energy, which can realize the adsorption-resolution process efficiently. 2) It has high stability, does not react with the analyte and produce strong background mass spectrometry signals. 3) It can be uniformly deposited on the sample target to ensure the reproducibility of the test and avoid matrix aggregation and sweet spot effects [38]. To demonstrate the feasibility of using the novel MOF@MOF matrix in MALDI-TOF-MS analysis, its analytical performance was compared with the most commonly used traditional organic matrices (DHB, SA, and THAP) in the positive-ion detection mode. Fig. S2 shows the optical images of different matrix dispersed on the stainless-steel target. The MOF@MOF matrix (Figs. S2e–f) demonstrates a homogeneous crystal layer that can prevent variability in signal strength from different locations on the target surface and improve the point-to-point reproducibility. On the other hand, the direct analysis result of EMO (Fig. S3a) presents a low ionization efficiency and a complicated background in the absence of matrix. Furthermore, using the traditional organic matrices, such as DHB, SA, and THAP, also displays a poor performance (Figs. S3b–d). However, using the MOF@MOF material with adsorption treatment has a higher analyte's signal intensity and less background interference, showing the characteristic MS fragments at *m/z* 271 ($[M+H]^+$), 293 ($[M+Na]^+$), and 309 ($[M+K]^+$) of EMO (Fig. S2f).

3.3. Optimization of experimental conditions

The low laser intensity will result in a weak sample signal intensity of low signal-to-noise ratio (SNR). However, the increasing laser intensity will enhance both the sample signal and background interference. As a result, the optimal SNR is obtained when the laser intensity is 30%, which was selected to satisfy the analysis requirements.

To obtain optimal enrichment efficiency, the effects of incubation time, incubation temperature, and the amount of adsorbent on the signal intensity of RAs were systematically investigated. Due to the high porosity of MOF material, a fast adsorption equilibrium can be achieved. Therefore, the effect of incubation time was investigated in the range of 2–12 min. As shown in Fig. 3a, the MS signals of RAs at 2−8 min are relatively weaker than that of 10 min and 12 min, and 10 min is enough for the incubation, which was finally chosen. Similar results can be observed in the investigation of temperature from 20 °C to 45 °C (Fig. 3b). Herein, 40 °C was applied in the following experiments.

The amount of MOF@MOF plays a critical role in the improvement of intensity of RAs MS signals. Therefore, the amount of MOF@MOF within the range of 25–150 μg was investigated. Fig. 3c illustrates that the MS signals increase significantly with the increase in material amounts from 25 μg to 100 μg, but the MS signals decrease sharply when the material amount is exceeded 100 μg, which may be due to the matrix thickness of the same spot [39]. Thus, 100 μg of MOF@MOF was adopted as the optimum amount of material.

3.4. Storage stability, salt tolerance, and applicability of the MOF@MOF in MALDI-TOF-MS analysis

The EMO (0.25 μg/mL) was employed as a model analyte to evaluate the storage stability and salt tolerance of the prepared material. MOF@MOF was stored at room temperature for six weeks and the storage stability was studied by measuring the $[M+H]^+$ intensity of EMO at different time points. Fig. 3d shows that long-term storage of the material has no significant influence on the MS signals of EMO with relative standard deviation (RSD) less than 5.4%. In the ideal state, the structural unit of UiO-66 is composed of $[Zr_6O_4(OH)_4]$ metal clusters ligated to $12H_2BDC$, which is the highest number of organic ligand-metal cluster coordination available in MOFs. The dense structural unit makes the whole structure stably connected. In addition, the Zr is highly oxygenophilic, the strong Zr–O bond in the UiO-66 structure also increases its stability [40].

Biological samples usually contain high concentrations of salts, which will lead to a low ionization efficiency and suppress the analytes' MS signals. To explore the salt tolerance of the material, the $[M+Na]^+$ intensity of EMO in positive ion mode was determined and compared by adding 0−150 mM of NaCl solution. The results (Fig. S4) show that even the NaCl concentration reaches at 150 mM, a slight decline by less than 17.4% of the initial intensity is observed, which indicates that the MOF@MOF matrix significantly improved the salt tolerance of MALDI-TOF-MS analysis. In addition, with the addition of NaCl, the $[M+K]^+$ signals of EMO are significantly suppressed, making the spectra simpler.

To explore the applicability of the MALDI-TOF-MS method using MOF@MOF as a matrix in the analysis of other small-molecule compounds, several compounds, such as amino acids (tyrosine, glutamic acid, phenylalanine, and histidine), flavone (naringenin and hesperetin), phenolic acid (rosmarinic acid), coumarin (psoralen), and diterpene quinone (tanshinone IIA), were analyzed. From the results that are shown in Fig. S5, the sodium adduct and potassium adduct signals for all compounds are presented in the spectra. The glutamic acid, phenylalanine, and psoralen present the most sensitive detection based on the comparisons of the characteristic peaks obtained at the same concentration.

Table 1
The results of method validation using MOF@MOF as the adsorbent and matrix.

Analytes	Regressive curves	Liner range (ng/mL)	R^2	LOD (ng/mL)	LOQ (ng/mL)	RSD (%) (n = 6)
EMO	y = 9349.11x+211.91	62.5–1000	0.990	3.15	10.49	9.9
CHR	y = 9085.78x+11.18	62.5–1000	0.991	4.90	16.34	6.9
PHY	y = 8354.26x+1.25	62.5–1000	0.991	4.68	15.61	8.3

EMO, emodin; CHR, chrysophanol; PHY, physcion.

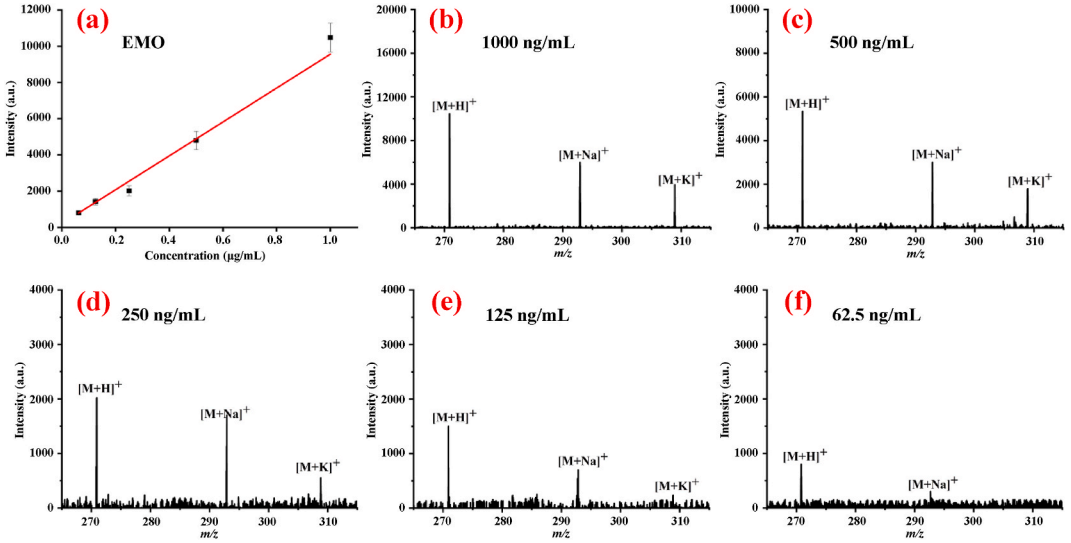

Fig. 4. (**a**) The calibration plot of EMO ($[M+H]^+$ at m/z 271) after enrichment treatment using UiO-66-$(OH)_2$@UiO-66-NH_2 as the adsorbent and matrix (n = 3); Mass spectra of EMO with different concentrations of (**b**)1000, (**c**) 500, (**d**) 250, (**e**) 125, and (**f**) 62.5 ng/mL after enrichment treatment. EMO, emodin.

Table 2
Recoveries of EMO, CHR, and PHY using UiO-66-$(OH)_2$@UiO-66-NH_2 as adsorbent and matrix after enrichment treatment in spiked rabbit plasma samples (n = 3).

Spiked (ng/mL)	EMO		CHR		PHY	
	RSD (%)	Recovery (%)	RSD (%)	Recovery (%)	RSD (%)	Recovery (%)
100	4.7	101.5	8.1	99.4	7.4	95.3
200	8.1	96.4	3.9	95.2	5.4	99.4
800	9.1	95.8	9.9	88.3	9.5	90.2

EMO, emodin; CHR, chrysophanol; PHY, physcion.

3.5. Quantitative analysis of RAs in serum sample

The MALDI-TOF-MS method using MOF@MOF as an adsorbent and matrix was applied in the quantitative analysis of RAs. The linear range, correlation coefficient, limit of detection (LOD), limit of quantification (LOQ), and repeatability of the method were determined under the optimized conditions. All measurements were repeated three times (n = 3). The LOD was determined as a signal-to-noise ratio (S/N) equal to 3, and the LOQ was determined as a S/N equal to 10. The repeatability was carried out by analyzing the individual sample solution six times. The results of direct analysis and enrichment treatment are shown in Table S1 and Table 1, respectively. After the enrichment treatment, good linear relationship and lower LODs are obtained. The intensity of $[M+H]^+$ of RAs increase linearly within the concentration range of 62.5–1000 ng/mL ($R^2 \geq 0.990$). The LODs (S/N = 3) for RAs are between 3.15 ng/mL and 4.90 ng/mL. The precision was evaluated by six repeated analysis of 250 ng/mL of RAs, and the RSD is in the range of 6.9–9.9%. More details of the calibration plots and mass spectra of RAs are shown in Fig. 4 and Figs. S6–S10.

The applicability and accuracy of this method in real plasma sample analysis were investigated through the recovery study. The contents of RAs in spiked rabbit plasma samples were determined and the results are summarized in Table 2. The rabbit plasma, which is a biological product, was purchased from Shanghai YuanYe Biological Technology Co., Ltd. All the analysis was performed in triplicates. The recoveries of various spiked concentrations (100, 200, and 800 ng/mL) of samples are in the range of 88.3–101.5% with RSD ≤9.9%, which further demonstrate the exceptional performance of the MOF@MOF matrix in the determination of RAs.

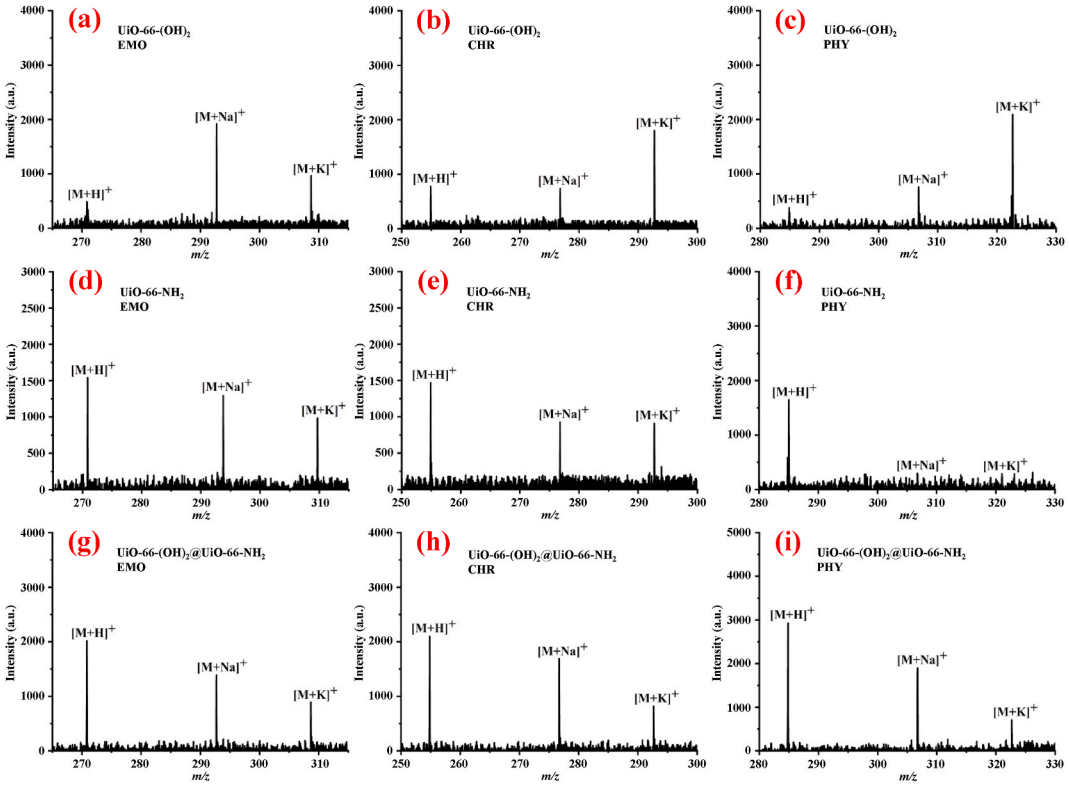

Fig. 5. Mass spectra of 250 ng/mL of EMO using (**a**) UiO-66-$(OH)_2$, (**d**) UiO-66-NH_2, and (**g**) UiO-66-$(OH)_2$@UiO-66-NH_2 as adsorbent and matrix; Mass spectra of 250 ng/mL of CHR using (**b**) UiO-66-$(OH)_2$, (**e**) UiO-66-NH_2, and (**h**) UiO-66-$(OH)_2$@UiO-66-NH_2 as adsorbent and matrix; Mass spectra of 250 ng/mL of PHY using (**c**) UiO-66-$(OH)_2$, (**f**) UiO-66-NH_2, and (**i**) UiO-66-$(OH)_2$@UiO-66-NH_2 as adsorbent and matrix, respectively. EMO, emodin; CHR, chrysophanol; PHY, physcion.

3.6. Mechanism investigation

To further demonstrate the characteristics of the prepared MOF@MOF material, the MALDI-TOF-MS analysis of RAs using different matrices were compared. As shown in Fig. 5, the characteristic $[M+H]^+$, $[M+Na]^+$, and $[M+K]^+$ adduct peaks of RAs are observed in all mass spectra. Furthermore, using MOF@MOF as MALDI matrix displays a higher sensitivity to RAs in positive ion mode, obtaining enhanced analyte signals with low background interference, which may be related to the strong adsorption performance of the core-shell structure MOF material. For further comparison, the adsorption capacity of the three MOF materials was evaluated by solid-phase extraction coupled with HPLC analysis. The results are shown in Table S2 and the relevant chromatograms are displayed in Fig. S11. The highest adsorption capacity for the analysis of RAs is obtained using MOF@MOF as adsorbent, whose adsorption capacity to EMO is calculated to be 6.40 μg/mg when the concentration of analyte is 20 μg/mL.

The excellent performance of MOF@MOF as an adsorbent and matrix can be attributed to the following two main reasons. 1) There are abundant polar hydroxyl groups and anthraquinone structure in the molecules of RAs. In this study, TPA-$(OH)_2$ and TPA-NH_2 were adopted as functional ligands for preparing the MOF@MOF, which contains many functional groups including benzene ring, amino, and hydroxyl. Consequently, multiple interaction effects such as hydrogen-bonding, dipolar-dipolar and π-π conjugation are involved in the enrichment process. 2) The efficient absorption of energy at laser wavelength and transfer the energy to analyte is a prerequisite of an ideal MALDI matrix. From the UV–Vis spectrum displayed in Fig. S12, MOF@MOF shows strong UV absorption in the range of 250–800 nm. In addition, the phenyl rings of MOF@MOF can provide abundant π-π and C–H/π interactions to hydroxyl and electron-rich anthraquinone structure, which can promote the proton transfer from the matrix to the RAs during the ionization process.

4. Conclusions

In summary, a core-shell structure MOF@MOF composite was prepared and used as an adsorbent and matrix for the sensitive MALDI-TOF-MS quantitative analysis of RAs. Compared with traditional matrices, MOF@MOF shows the advantages of low background interference in the low-mass range, high sensitivity, satisfactory salt tolerance, and good storage stability. Moreover, the developed MALDI-TOF-MS method using MOF@MOF as a matrix was successfully applied in the determination of RAs in spiked rabbit plasma samples. This work provides a reference for designing multifunctional matrix for the enrichment and accurate quantification of small-molecule compounds by MALDI-TOF-MS analysis.

Author contribution statement

Shi-Jun Yin: Conceived and designed the experiments; Performed the experiments; Analyzed and interpreted the data; Wrote the paper.

Hua Chen: Conceived and designed the experiments; Analyzed and interpreted the data; Contributed reagents, materials, analysis tools or data.

Shengpeng Wang: Conceived and designed the experiments; Contributed reagents, materials, analysis tools or data.

Yitao Wang: Contributed reagents, materials, analysis tools or data.

Fengqing Yang: Conceived and designed the experiments; Analyzed and interpreted the data; Contributed reagents, materials, analysis tools or data; Wrote the paper.

Data availability statement

Data included in article/supp. material/referenced in article.

Institutional review board statement

The rabbit plasma used in this study, which is a biological product, was purchased from Shanghai YuanYe Biological Technology Co., Ltd. Thus, not applicable to an Ethics statement.

Declaration of competing interest

The authors declare that they have no known competing financial interests or personal relationships that could have appeared to influence the work reported in this paper.

Acknowledgements

This work is supported by the Open Research Project Program of the State Key Laboratory of Quality Research in Chinese Medicine (University of Macau) (Ref. No.: SKL-QRCM-OP21005).

Appendix A. Supplementary data

Supplementary data to this article can be found online at https://doi.org/10.1016/j.heliyon.2023.e16245.

References

[1] F. Levander, P. James, Automated protein identification by the combination of MALDI MS and MS/MS spectra from different instruments, J. Proteome Res. 4 (1) (2005) 71–74.
[2] J. McMillen, D. Gutierrez, A. Judd, J. Spraggins, R. Caprioli, Enhancement of tryptic peptide signals from tissue sections using MALDI IMS post ionization (MALDI-2), J. Am. Soc. Mass Spectrom. 32 (10) (2021) 2583–2591.
[3] Y. Nakashima, M. Setou, Distribution of antisense oligonucleotides in rat eyeballs using MALDI imaging mass spectrometry, Mass Spectrom. 7 (1) (2018) A0070.
[4] Z.X. Wang, Q.Q. Zhang, H.L. Shen, P.Y. Yang, X.W. Zhou, Optimized MALDI-TOF MS strategy for characterizing polymers, Front. Chem. 9 (2021), 698297.
[5] S. Kim, S. Kwon, Y. Kim, Graphene oxide derivatives and their nanohybrid structures for laser desorption/ionization time-of-flight mass spectrometry analysis of small molecules, Nanomaterials 11 (2) (2021) 288.
[6] U. Conway, A. Warren, C. Arthur, P. Gates, A study of the application of graphite MALDI to the analysis of short-chain polyethylene glycols, Polym. Chem. 12 (3) (2021) 439–448.
[7] S. Maghari, E. Reimhult, P. Ghezellou, A. Ghassempour, Modifying superparamagnetic iron oxide and silica nanoparticles surfaces for efficient (MA)LDI-MS analyses of peptides and proteins, Rapid Commun. Mass Spectrom. 36 (1) (2021), e9212.
[8] S. Li, J.A. Liu, J.P. Sun, Z.P. Wang, K. Wang, L. Guo, S.L. Yang, J.C. Wei, X.J. Zheng, Z.W. Zhao, Co-NC as adsorbent and matrix providing the ability of MALDI MS to analyze volatile compounds, Chin. Chem. Lett. 32 (1) (2021) 62–65.
[9] H. Li, T. Li, X.Z. Shi, G.W. Xu, Recent development of nanoparticle-assisted metabolites analysis with mass spectrometry, J. Chromatogr. A 1636 (2021), 461785.
[10] X. Han, D. Li, S. Wang, Y. Lin, Y. Liu, L. Lin, L. Qiao, Serum amino acids quantification by plasmonic colloidosome-coupled MALDI-TOF MS for triple-negative breast cancer diagnosis, Mater. Today Bio 17 (2022), 100486.
[11] Z. Qiu, Z. Zheng, Z. Song, Y. Sun, Q. Shan, Z. Lin, Z. Xie, Co_3O_4 nanocrystals as matrices for the detection of amino acids, harmful additives and pesticide residues by MALDI-TOF MS, Talanta 242 (2022), 123299.
[12] H. Daglar, I. Erucar, S. Keskin, Recent advances in simulating gas permeation through MOF membranes, Adv. Mater. 2 (16) (2021) 5300–5317.
[13] R. Yan, T. Ma, M.H. Cheng, X.F. Tao, Z. Yang, F. Ran, S. Li, B. Yin, C. Cheng, W. Yang, Metal-organic-framework-derived nanostructures as multifaceted electrodes in metal-sulfur batteries, Adv. Mater. 33 (27) (2021), e2008784.
[14] Y. Shen, T. Pan, L. Wang, Z. Ren, W. Zhang, F.W. Huo, Programmable logic in metal-organic frameworks for catalysis, Adv. Mater. 33 (46) (2021), e2007442.
[15] L. Chai, J.Q. Pan, Y. Hu, J.J. Qian, M.C. Hong, Rational design and growth of MOF-on-MOF heterostructures, Small 17 (36) (2021), e2100607.
[16] M.X. Lu, Y.J. Deng, Y.C. Li, T.B. Li, J. Xu, S.W. Chen, J.Y. Wang, Core-shell MOF@MOF composites for sensitive nonenzymatic glucose sensing in human serum, Anal. Chim. Acta 1110 (2020) 35–43.
[17] R. Rolta, V. Kumar, A. Sourirajan, N. Upadhyay, K. Dev, Bioassay guided fractionation of rhizome extract of Rheum emodi wall as bio-availability enhancer of antibiotics against bacterial and fungal pathogens, J. Ethnopharmacol. 257 (2020), 112867.

[18] M. Rokaya, Z. Münzbergová, B. Timsina, K. Bhattarai, Rheum australe D. Don: a review of its botany, ethnobotany, phytochemistry and pharmacology, J. Ethnopharmacol. 141 (3) (2012) 761–774.
[19] L.J. Liu, J. Zou, X. Liu, L.H. Jiang, J.Y. Li, Inhibition of ATP-induced macrophage death by emodin via antagonizing P2X7 receptor, Eur. J. Pharmacol. 640 (1–3) (2010) 15–19.
[20] Y.M. Li, B.C. Li, P. Li, J.Z. Liu, J.L. Cui, Z.Q. Mei, Effects of Na-FA on gastrointestinal movement and gastric ulcer in mice, Zhong Yao Cai 34 (10) (2011) 1565–1569.
[21] X. You, S. Feng, S. Luo, D. Cong, Z. Yu, Z. Yang, J. Zhang, Studies on a rhein-producing endophytic fungus isolated from *Rheum palmatum* L, Fitoterapia 85 (2013) 161–168.
[22] Y. Cheng, H. Zhang, L. Qu, Y. He, M.N. Routledge, Y. Yun Gong, B. Qiao, Identification of rhein as the metabolite responsible for toxicity of rhubarb anthraquinones, Food Chem. 331 (2020), 127363.
[23] S.Z. Xu, G.J. Yang, F. Feng, Investigation of distinction chemical markers for Rhubarb authentication based on high-performance liquid chromatography-time-of-flight mass spectrometry and multivariate statistical analysis, Food Anal. Methods 10 (2017) 3934–3946.
[24] X.Y. Shang, Z.B. Yuan, Separation of effective constituents from Rhubarb by micellar electrokinetic capillary chromatograph, Anal. Lett. 31 (2002) 203–214.
[25] L.S. Luo, W.S. Lo, X.M. Si, H.L. Li, Y.C. Wu, Y.Y. An, Q.L. Zhu, L.Y. Chou, T. Li, C.K. Tsung, Directional engraving within single crystalline metal-organic framework particles via oxidative linker cleaving, J. Am. Chem. Soc. 141 (2019) 20365–20370.
[26] S. Kulandaivel, W.C. Lo, C.H. Lin, Y.C. Yeh, Cu-PyC MOF with oxidoreductase-like catalytic activity boosting colorimetric detection of Cr(VI) on paper, Anal. Chim. Acta 1227 (2022), 340335.
[27] M. Mansouri, S. Sadeghian, G. Mansouri, N. Setareshenas, Enhanced photocatalytic performance of UiO-66-NH_2/TiO_2 composite for dye degradation, Environ. Sci. Pollut. Res. Int. 28 (20) (2021) 25552–25565.
[28] Y.Z. Sun, M. Chen, H. Liu, Y. Zhu, D.B. Wang, M. Yan, Adsorptive removal of dye and antibiotic from water with functionalized zirconium-based metal organic framework and graphene oxide composite nanomaterial UiO-66-$(OH)_2$/GO, Appl. Surf. Sci. 525 (2020), 146614.
[29] J. Yang, B. Ruan, W. Ni, L. Tsai, N. Ma, D. Shi, T. Jiang, F. Tsai, UiO-66-$(OH)_2$ derived porous fluorescence tunable materials by doping with carbon dots, ECS J. Solid State Sci. Technol. 10 (2021), 106011.
[30] Z. Moghaddam, M. Kaykhaii, M. Khajeh, A. Oveisi, Synthesis of UiO-66-OH zirconium metal-organic framework and its application for selective extraction and trace determination of thorium in water samples by spectrophotometry, Spectrochim. Acta Mol. Biomol. Spectrosc. 194 (2018) 76–82.
[31] S.S. Chen, J. Liu, Y.F. Xu, Z. Li, T. Wang, J. Xu, Z. Wang, Hydrogen storage properties of the novel crosslinked UiO-66-$(OH)_2$, Int. J. Hydrogen Energy 43 (32) (2018) 15370–15377.
[32] S. Subudhi, G. Swain, S. Tripathy, K. Parida, UiO-66-NH_2 metal-organic frameworks with embedded MoS_2 nanoflakes for visible-light-mediated H_2 and O_2 evolution, Inorg. Chem. 59 (14) (2020) 9824–9837.
[33] Y.F. Wu, Y. Xiao, H. Yuan, Z.Q. Zhang, S.B. Shi, R.P. Wei, L.J. Gao, G.M. Xiao, Imidazolium ionic liquid functionalized UiO-66-NH_2 as highly efficient catalysts for chemical fixation of CO_2 into cyclic carbonates, Microporous Mesoporous Mater. 310 (2021), 110578.
[34] F. Zhao, C.H. Su, W.X. Yang, Y. Han, X.L. Luo, C.H. Li, W.Z. Tang, T.L. Yue, Z.H. Li, In-situ growth of UiO-66-NH_2 onto polyacrylamide-grafted nonwoven fabric for highly efficient Pb(II) removal, Appl. Surf. Sci. 527 (2020), 146862.
[35] Q.Q. Guan, B. Wang, X.S. Chai, J. Liu, J.J. Gu, P. Ning, Comparison of Pd-UiO-66 and Pd-UiO-66-NH_2 catalysts performance for phenol hydrogenation in aqueous medium, Fuel 205 (2017) 130–141.
[36] R. Ediati, W. Aulia, B. Nikmatin, A. Hidayat, U. Fitriana, C. Muarifah, D. Sulistiono, F. Martak, D. Prasetyoko, Chitosan/UiO-66 composites as high-performance adsorbents for the removal of methyl orange in aqueous solution, Mater. Today Chem. 21 (2021), 100533.
[37] V. Butova, O. Burachevskaya, M. Muratidi, I. Surzhikova, P. Zolotukhin, P. Medvedev, I. Gorban, A. Kuzharov, M. Soldatov, Loading of the model amino acid leucine in UiO-66 and UiO-66-NH_2: optimization of metal-organic framework carriers and evaluation of host-guest interactions, Inorg. Chem. 60 (8) (2021) 5694–5703.
[38] X.Y. Chen, Y.H. Wang, S.Y. Ren, S. Li, Y. Wang, K. Qin, S. Li, D.P. Han, Y. Peng, T. Han, Z.X. Gao, B.X. Gao, H.Y. Zhou, Amorphous poly-*N*-vinylcarbazole polymer as a novel matrix for the determination of low molecular weight compounds by MALDI-TOF MS, RSC Adv. 12 (24) (2022) 15215–15221.
[39] Y.C. Yang, Y. Xia, Self-assembled matrix fabricated by Fe-metal organic frameworks and carboxymethyl cellulose for the determination of small molecules by MALDI-TOF MS, Mikrochim. Acta 187 (8) (2020) 445.
[40] N.A. Ramsahye, J. Gao, H. Jobic, P.L. Llewellyn, Q. Yang, A.D. Wiersum, M.M. Koza, V. Guillerm, C. Serre, C.L. Zhong, G. Maurin, Adsorption and diffusion of light hydrocatbons in UiO-66(Zr): a combination of experimental and modeling tools, J. Phys. Chem. C 118 (2014) 27470–27482.